ARTICLES
PUBLISHED ONLINE: 8 AUGUST 2010 | DOI: 10.1038/NCHEM.761
nature chemistry

Efficient water oxidation at carbon nanotube–polyoxometalate electrocatalytic interfaces

Francesca M. Toma[1,2], Andrea Sartorel[3], Matteo Iurlo[4], Mauro Carraro[3], Pietro Parisse[2,5], Chiara Maccato[3], Stefania Rapino[4], Benito Rodriguez Gonzalez[6], Heinz Amenitsch[7], Tatiana Da Ros[1], Loredana Casalis[2,5], Andrea Goldoni[5], Massimo Marcaccio[4], Gianfranco Scorrano[3], Giacinto Scoles[2], Francesco Paolucci[4], Maurizio Prato[1]* and Marcella Bonchio[3]*

Water is the renewable, bulk chemical that nature uses to enable carbohydrate production from carbon dioxide. The dream goal of energy research is to transpose this incredibly efficient process and make an artificial device whereby the catalytic splitting of water is finalized to give a continuous production of oxygen and hydrogen. Success in this task would guarantee the generation of hydrogen as a carbon-free fuel to satisfy our energy demands at no environmental cost. Here we show that very efficient and stable nanostructured, oxygen-evolving anodes are obtained by the assembly of an oxygen-evolving polyoxometalate cluster (a totally inorganic ruthenium catalyst) with a conducting bed of multiwalled carbon nanotubes. Our bioinspired electrode addresses the one major challenge of artificial photosynthesis, namely efficient water oxidation, which brings us closer to being able to power the planet with carbon-free fuels.

Molecular hydrogen has the potential to quench the world's clean-energy thirst and can, in principle, be made by the chemical splitting of a water molecule into its gaseous components, hydrogen and oxygen[1]. In practice, production of hydrogen is hindered by the remarkable stability of water itself, because the free energy (ΔG) required for the overall process $2H_2O \rightarrow 2H_2 + O_2$ amounts to 113.38 kcal (4.92 eV) (refs 1–3). The challenge lies mainly in the formidable complexity of the oxidative half-reaction $2H_2O \rightarrow O_2 + 4H^+ + 4e^-$, in which the release of diatomic O_2 involves an overall four-electron/four-proton process with the final formation of an oxygen–oxygen bond[4].

At the heart of the natural enzyme photosystem II, water oxidation is accomplished by a metal–oxygen cluster with four manganese and one calcium atom, Mn_4Ca (refs 5–7). The adoption of a catalytic core that features adjacent transition-metal centres and multiple μ-hydroxo–oxo bridging units is a winning strategy devised by nature to effect multiple cascade transformations with a high efficiency and minimal energy cost[8]. Even the chloroplast-embedded Mn_4Ca catalyst finds it difficult, however, to oxidize water under ambient conditions. Indeed, photosystem II works with a moderate overpotential (η) of about 0.3–0.4 V at physiological pH conditions[9]. Under such conditions, oxygen turnover inflicts lethal damage to the natural protein environment, which needs to be replaced by the organism every 30 minutes through a self-healing mechanism[10]. As a consequence, the design of a water-splitting synthetic centre that mimics nature is a formidable challenge, because of the need for a functional but stable catalyst.

A promising innovation in the field is the recent discovery of a totally inorganic and highly robust tetraruthenate cluster, which belongs to the class of polyoxometalate (POM) anions $M_{10}[Ru_4(H_2O)_4(\mu\text{-}O)_4(\mu\text{-}OH)_2\ (\gamma\text{-}SiW_{10}O_{36})_2]$ (**M_{10}1**, M = Cs, Li). This complex has oxygen-evolving activity, features a multimetal oxide structure and nanoscale dimensions, and is obtained easily in high yields and gram quantities[11,12]. Water oxidation catalysis by **1** occurs in the presence of Ce(IV), introduced as a sacrificial oxidant, with a remarkably high turnover frequency (TOF, the turnover number (TON) per unit time) of 450 cycles h^{-1} and no deactivation. In this process, the four Ru(IV)–H_2O groups within the catalyst core are able to mediate the four-electron/four-proton overall process through a sequential electron and proton loss in a relatively narrow potential range (redox potential levelling)[13,14]. We show that such flexibility, together with the unique mechanistic and stability features of **1**, can leverage important improvements in the catalytic protocol at the heterogeneous surface of functional electrodes.

Results and discussion

Fabrication of nanostructured oxygen-evolving anodes (OEAs). State-of-the-art water electrolysers operate with medium-to-high overpotential. A promising alternative is based on the immobilization of oxygen-evolving molecular catalysts on electrodes, with a few proof-of-principle examples available so far[15–17]. We show that our new nanostructured anodes (Fig. 1) perform water oxidation with an overpotential as low as 0.35 V and TOFs that approach those of solution behaviour (up to 300 h^{-1}). Our approach was to improve the electrical contact between the redox-active centre and the surface of the electrode using multiwalled carbon nanotubes (MWCNTs) (Fig. 1a). These serve as conductive nanowire scaffolds to:

- provide heterogeneous support to **1**;
- control the material morphology;
- increase the surface area;
- funnel the sequential electron transfer to the electrode, and thus favour energy dispersion and relieve catalytic fatigue.

[1]Center of Excellence for Nanostructured Materials (CENMAT), INSTM, Dipartimento di Scienze Farmaceutiche, Università di Trieste, Piazzale Europa 1, 34127 Trieste, Italy, [2]SISSA-ELETTRA NanoInnovation Lab, SISSA-ISAS, via Beirut 2–4, 34151 Trieste, Italy, [3]ITM-CNR and Dipartimento di Scienze Chimiche, Università di Padova, via Marzolo 1, 35131 Padova, Italy, [4]Dipartimento di Chimica, Università di Bologna, Italy, via Selmi 2, 40126 Bologna, Italy, [5]Sincrotrone Trieste SCpA, SS14 Km 163, 5 Area Science Park, Basovizza, 34149 Trieste, Italy, [6]CACTI Universidade de Vigo, Campus Universitario Lagoas-Marcosende ES-36310 Vigo, Spain, [7]Institute of Biophysics and Nanosystems Research, Austrian Academy of Sciences, Schmiedlstrasse 6, 8042-Graz, Austria.
*e-mail: prato@units.it; marcella.bonchio@unipd.it

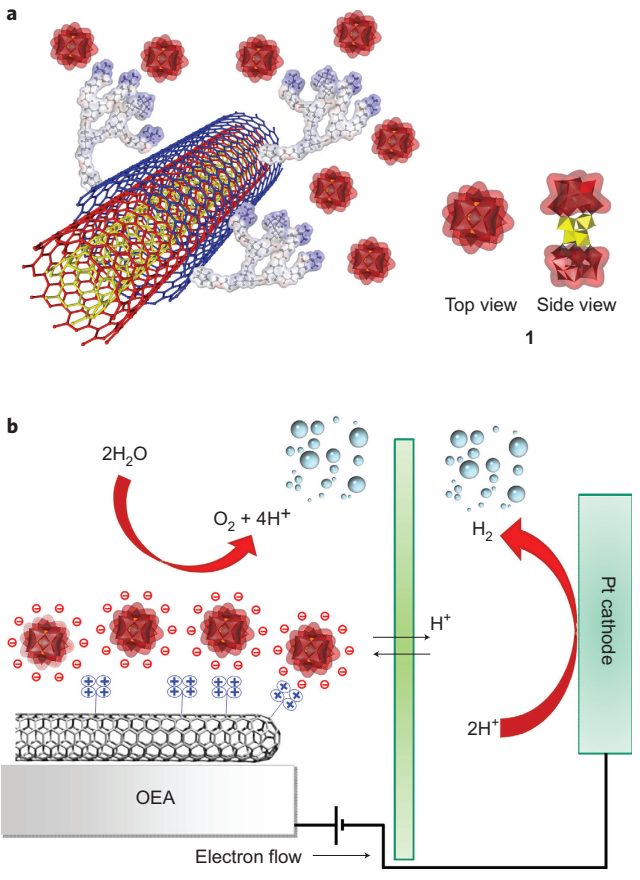

Figure 1 | Nanostructured oxygen-evolving material. a, Electrostatic capture of polyanionic ruthenium-containing clusters **1** (negatively charged, red surface) by polycationic dendrons on the MWCNT surface (positively charged, blue surface) and polyhedric structure showing the side and front view of the POM (red)-embedded tetraruthenate core of **1** (yellow). **b**, General scheme for a water-splitting electrocatalytic cell with the integrated nanostructured OEA.

For enzyme-based fuel cells, carbon nanotubes (CNTs) were employed successfully to increase the enzyme loading on the electrode with an extended three-dimensional space built by an electrically conducting network of high surface area[18]. Furthermore, the good mechanical properties and superb thermal stability with the processability on chemical functionalization provided additional advantages to the fabrication of CNT-based electrodes[19]. The assembly of organic and inorganic domains to yield **1@MWCNT** was achieved through electrostatic scavenging (Fig. 1 and Supplementary Scheme S1) at pH 5 by exposure of $\mathbf{Li_{10}1}$ to water-soluble MWCNTs decorated with polyamidoamine (PAMAM) ammonium dendrimers (**MWCNT-dend**) (ref. 20). Thermogravimetric analysis (TGA, Supplementary Fig. S1) carried out for both the initial **MWCNT-dend** and the hybrid product provided a direct estimate of the catalyst loading within the composite **1@MWCNT** (Supplementary Table S1).

Association of **1** with **MWCNT-dend** yielded an effective catalyst loading in the range 0.07–0.1 mmol g^{-1}, consistent with saturation of the positive charges of the MWCNT scaffold. Assembly of **1** on pristine MWCNTs gave negligible catalyst loading (see below), which thus confirmed the key role of the electrostatic interaction with the attached dendrimer chains. The hybrid composite **1@MWCNT** was characterized further by a variety of spectroscopy and microscopy techniques, including resonant Raman, small-angle X-ray scattering (SAXS), scanning transmission electron microscopy (STEM), X-ray dispersive energy spectroscopy (XEDS) and high-resolution transmission electron microscopy (HRTEM). The resonant Raman features of **1** in the pure state and on the CNT hybrid are strikingly similar, which indicates that the structure of **1** was preserved during and after the assembly process (Fig. 2a). In particular, the prominent bands in the range 250–500 cm^{-1} were assigned to Ru-(H_2O) stretching modes (250–400 cm^{-1}) and vibrations of the Ru_4 core were found at 450–500 cm^{-1} (ref. 13). This region was totally silent for pristine MWCNTs exposed to **1**. Furthermore, the expected MWCNT D and G bands and its overtone were observed at 1,350, 1,600 and 2,720 cm^{-1}, respectively, in the spectrum of **1@MWCNT**.

SAXS diffraction patterns were obtained and analysed for both **MWCNT-dend** and **1@MWCNT** (both at pH 5.5, 0.5 mg ml^{-1}), and compared with the solution behaviour of $\mathbf{Li_{10}1}$ in water (pH 5.5, 1 mg ml^{-1}). The scattering pattern observed in solution for $\mathbf{Li_{10}1}$ (Fig. 2b, blue curve) and the simulated curve were consistent with the geometry of the isolated molecule (see Supplementary Information)[11]. The solution study gave a nearest-neighbour distance of 6 nm at 50 mg ml^{-1} (data not shown) and no indication of aggregation phenomena. Comparison of the experimental curves registered for **1@MWCNT** (Fig. 2b, black trace) and **MWCNT-dend** (Fig. 2b, red trace) showed that, in the observed regime, scattering from **1** dominated with respect to that from the MWCNT walls. Accordingly, the inorganic oxoclusters appeared to be deposited on the MWCNT surface mainly as single entities (nearest-neighbour distance was $d = 1.2$ nm), with a compact distribution driven by the positively charged, terminal functions of the dendron moiety. This is a key point to access single-site catalysis that approaches homogeneous behaviour.

The SAXS results were validated by *Z*-contrast STEM images of **1@MWCNT**, which showed individually separated molecules of **1** (bright spots, diameter 1–2 nm) on the CNT surface (Fig. 2c,d). STEM images gave a clear illustration of the electron-dense catalyst distribution on the nanotube surface. XEDS analysis showed the distribution of the ruthenium and tungsten elements that arose from the inorganic complex with respect to the carbon-based surface of the nanotube, as indicated by the colour-coded elemental map (Fig. 2e). The blue colour was assigned to the carbon Kα emission and the red colour to the tungsten Lα emission. Ruthenium from the embedded catalytic core was barely visible around 19 keV (Fig. 2e, inset). The distribution of tungsten was coincident with the brighter areas in the STEM images, which proved the localization of **1**. In addition, the HRTEM images showed that the surface of the CNT walls had a 2 nm thick catalyst coating (Fig. 2f). Extensive aggregation appeared to be localized mainly at the terminal sites of the nanotube, probably associated with a higher degree of covalent functionalization and thus a higher concentration of the positive dendron sites (Supplementary Fig. S9).

To evaluate the importance and role played by CNTs, **1** was assembled on amorphous carbon (AC) previously functionalized with the charged PAMAM dendron (**AC-dend**). The resulting material, **1@AC**, was characterized completely by TGA, HRTEM and STEM techniques (see Supplementary Information).

OEAs that integrated **1@MWCNT** were obtained on drop casting a water solution of the hybrid composite on indium tin oxide (ITO) electrodes (3 × 3 mm). Analysis of the resulting coating by X-ray photoelectron spectroscopy (XPS) revealed the expected tungsten $4f_{7/2}$ peak centred at 35.4 (±0.05) eV in binding energy, assigned to the W(VI) component of the POM framework[21], together with a ruthenium 3*d* peak observed in two distinct components, at 280.9 and 281.7 (±0.05) eV, attributed to high valent states[22].

Scanning electron microscopy (SEM) images of the electrode coating showed a highly porous three-dimensional extended network, built from interconnecting CNTs that carried catalyst **1** (Fig. 3a).

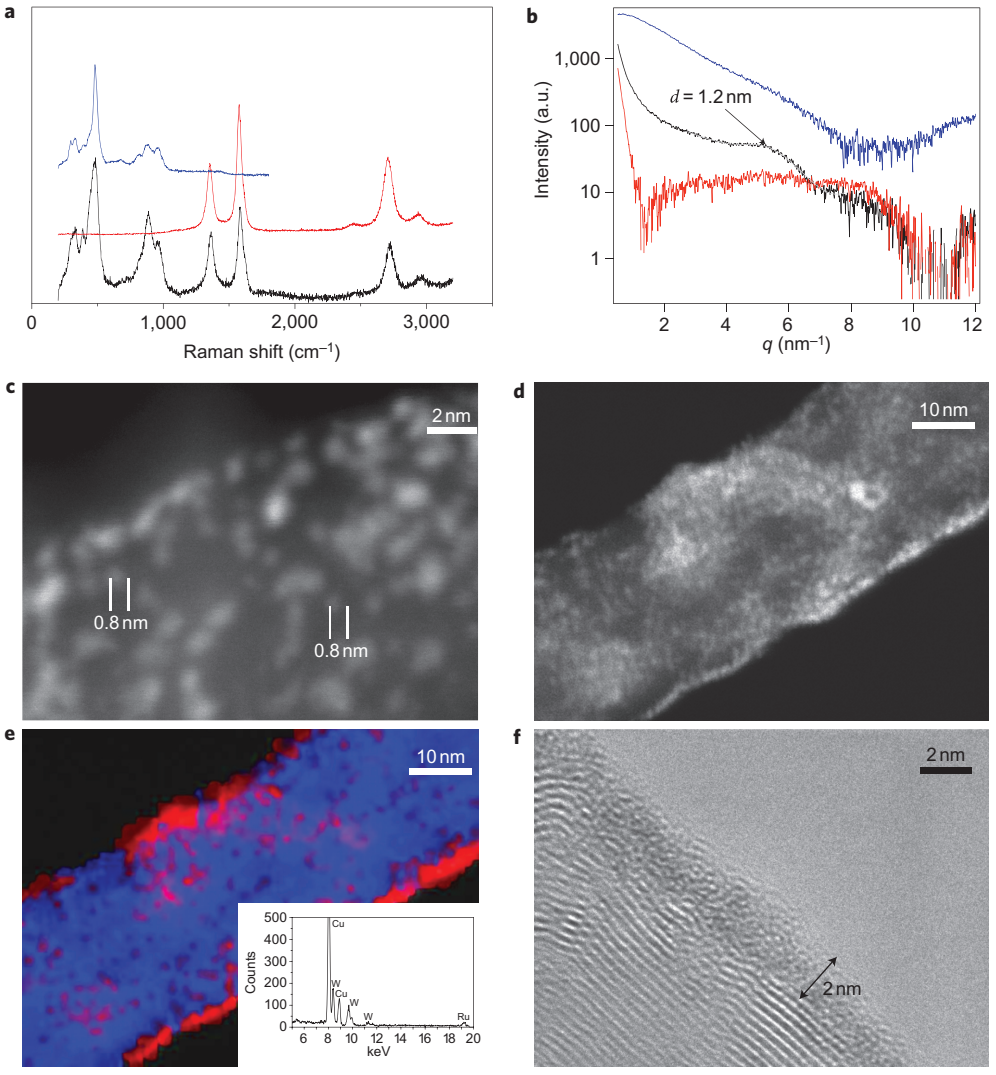

Figure 2 | Characterization of the composite 1@MWCNT. a, Resonant Raman spectra of **1@MWCNT** (black trace), pristine MWCNTs exposed to **1** (red trace) and crystalline **1** (blue trace). **b**, SAXS measurements (H_2O, pH 5.5) of **1@MWCNT** (black curve, 1 mg ml^{-1}) and fitting of the correlation peak (grey curve) with a *d*-spacing of about 1.2 nm, of **MWCNT-dend** (red curve, 1 mg ml^{-1}) and of **1** (blue curve, 0.5 mg ml^{-1}). *q* = scattering vector; a.u. = arbitrary units. **c**,**d**, *Z*-contrast STEM images in which the nanodomains (about 1 nm) ascribed to **1** yield a brighter contrast because of the presence of tungsten and ruthenium. **e**, XEDS elemental mapping of **1@MWCNT**, Kα_1 emission of carbon (blue) and Lα_1 emission of tungsten (red) show the presence of **1** at the surface of the nanotubes. The inset shows the semiquantitative microanalysis carried out on the same surface (copper peaks are caused by the grid of the transmission electron microscope). **f**, HRTEM of **1@MWCNT** at a higher magnification, which shows the presence of **1** (darker, unstructured zone 2 nm thick) in close contact with the MWCNT structure (layered structure).

The composite **1@MWCNT** possessed a high surface area and domains of nanometric dimensions that had an enhanced hydrophilic character because of the contemporary presence of tungsten and ruthenium sites and the charged nitrogen and oxygen residues, prone to assist water diffusion and stabilization through coordination and hydrogen-bonding interactions. Atomic force microscopy (AFM) measurements (Fig. 3b) provided direct evidence of the film roughness, which is associated with the effective surface area of the system. The two-dimensional AFM image of the electroactive layer on the ITO slabs was characterized by a granular-like texture that resulted in a highly porous material, as anticipated by SEM data. The root mean square (r.m.s.) roughness value, evaluated on the reported area of 10 × 10 μm, was 150 nm, notably higher than that of a flat silica sample, generally characterized by an r.m.s. ≈ 1 nm.

By a similar protocol, deposition of **1@AC** on ITO substrates gave doped anodes, the oxygen-evolving activity of which was used to benchmark that obtained with the **1@MWCNT** substrates (see below). According to STEM images (Supplementary Fig. S14), the distribution features of the POM nanodomains were very similar in both the carbon-based materials, and also displayed a vast coverage of the carbon matrix by a POM monolayer in the amorphous composite. Moreover, SEM evidence collected for the **1@AC** electrode confirmed the deposition of porous film with a globular matrix (see Supplementary Fig. S15). The observed close similarity of the morphology and surface properties for both composites (see Supplementary Information) allowed us to ascribe the electrocatalytic performance to the one-dimensional anisotropy and electronic properties of the nanostructured carbon-based matrix under examination.

Water oxidation electrocatalysis. The catalytic activity of the modified ITO electrodes was studied initially by cyclic voltammetry (CV) in a standard three-electrode cell, equipped with an Ag/AgCl reference electrode and a platinum-wire counter electrode, and containing an aqueous solution at pH 7 (phosphate buffer (PBS)), in air and at room temperature (Fig. 3c). As expected, the POM-free

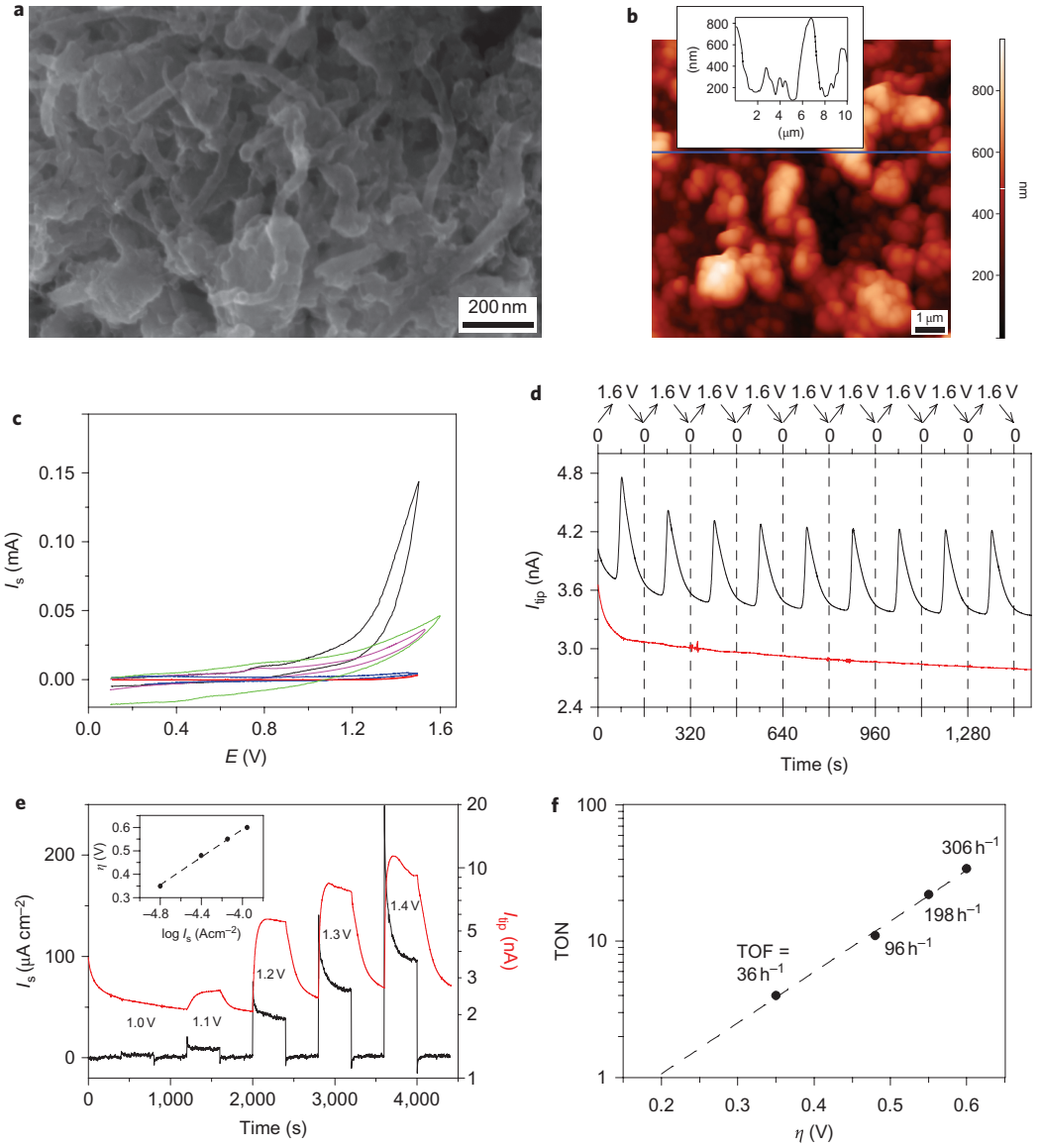

Figure 3 | Electroactive nanostructured ITO anodes. a, SEM image of a highly porous **1@MWCNT** film on ITO. **b**, AFM surface image of **1@MWCNT** on ITO (10 × 10 μm) and depth-profile sampling along the marked line in the AFM micrographs (inset). **c**, CV curves of ITO-deposited **1@MWCNT** (black trace), **1@AC** (green trace), **TBA1** (purple trace), **MWCNT-dend** (blue trace) and bare **ITO** (red trace) at pH 7. **d**, Current transients recorded at the SECM tip (μ-Clark) that display the O_2 production during nine sequential CV scans applied at **1@MWCNT** on the ITO (black line) or at the bare ITO substrate (red line) in H_2O at pH 7. **e**, Chronoamperometric current measured at the substrate (I_s, black trace) or at the μ-Clark (I_{tip}, red trace) on application of the potential waveform shown in Supplementary Fig. S19. The inset shows the quasi-stationary O_2 evolution current (measured at the substrate) versus overpotential curve ($\eta = E_{appl} - E^{\circ} - i_s \times R$, where E_{appl} is the potential applied to the catalyst (substrate) and E° the pH-dependent standard potential for H_2O oxidation (E° (V) (versus Ag/AgCl (3 M KCl)) = 1.02 − 0.059 × pH). **f**, Tafel plot showing TON and TOF as a function of overpotential η.

MWCNT-dend turned out to be catalytically inert (blue line in Fig. 3c and Supplementary Fig. S18). This was also the case for a sample of pristine MWCNTs, analysed before the divergent growth of the dendrimer, and thus confirmed the negligible voltammetric response of the POM-free material (Supplementary Fig. S18). The inherent metal content of MWCNT, therefore, did not contribute to the overall catalytic activity[23]. By contrast, ITO electrodes doped with **1** exhibited, in all cases, an oxidation wave at 0.9 V followed by the onset of a catalytic current at applied voltages >1.10 V caused by water oxidation[24]. With respect to oxygen production, the relative electrocatalytic activity of **1** on an ITO surface depended strongly on its environment and was in the order **1** < **1@AC** ≪ **1@MWCNT** (compare the purple, green and black curves in Fig. 3c). The lipophilic tetrabutyl ammonium salt of **1** was used in the deposition protocol on ITO.

The oxygen-evolving activity of **1@MWCNT** on ITO was assessed by scanning electrochemical microscopy (SECM) analysis, which allowed a faster determination of electrocatalytic efficiency with respect to bulk methods[25]. Figure 3d displays the O_2 production during nine CV scans between 0 and 1.6 V (versus an Ag/AgCl (3 M KCl) reference electrode) with a scan rate of 20 mV s^{-1}, applied at the ITO electrode doped with **1@MWCNT**. Thus, nine subsequent current transients were recorded at the SECM tip (μ-Clark) and showed an identical anodic performance on multicycle activity. Although this experiment does not guarantee the long-term durability of the electrode, this observation highlights the extreme robustness of the hybrid **1@MWCNT** nanocomposite, which leads to an excellent structural stability and retention of the electrocatalytic properties. The long-term durability needs to be addressed on an appropriately engineered electrode device[26].

Under the same conditions, bare ITO is totally inactive towards O_2 production (Fig. 2c, red trace).

The effective amount of electroactive catalyst deposited in the film (calculated as $n_{POM} = 8.3 \times 10^{-4}$ μmol according to Faraday's law; see Supplementary Information) and a quantitative analysis of oxygen production under electrocatalytic conditions was obtained from chronoamperometric experiments, in which the anodic potential (E_s) was stepped back and forth between 0 V and a positive value in the range 1.0–1.4 V (Supplementary Fig. S19) and the currents at either the doped ITO (I_s) or at the μ-Clark electrode (I_{tip}) were monitored continuously during the experiment (Fig. 3e). Under these conditions, the TON, expressed as the number of moles of generated oxygen per mole of electroactive catalyst on four-electron oxidation, can be derived from the integrated charges Q_s after subtraction of the contribution due to **1** ($Q_{POM} =$ 0.32 mC measured at 1 V, where no oxygen evolution is detected), according to equation (1) (see Supplementary Table S4):

$$\mathrm{TON} = \frac{n_{O_2}}{n_{POM}} = \frac{Q_s - Q_{POM}}{Q_{POM}} \quad (1)$$

TOF was then determined from the integration time τ (Supplementary Table S4), which yielded TOF values in the range 36–306 h^{-1}, depending on the applied overpotential. At pH 7.0, an appreciable catalytic current with a remarkable TOF (36 h^{-1}) was observed, initially at $\eta = 0.35$ V and reaching a peak performance of 306 h^{-1} at $\eta = 0.60$ V. The TOF efficiency is slightly inferior with respect to homogeneous conditions that employed Ce(IV) as the bulk oxidant[11]. This is a reasonable compromise because of the different experimental conditions and the transfer on a heterogeneous surface. However, the TOF from our electrode exceeded the values reported previously for Co- and Mn-based systems, which were in the range 0.7–20 h^{-1} at $\eta \geq 0.40$ V (refs 15–17). A peak TOF of 270 h^{-1} was reported for a cubane-like Mn_4O_4 catalytic core embedded in a Nafion membrane, which required both photoirradiation and electric power at an overpotential of 0.4 V. TOF in the range 20–270 h^{-1} was reported to depend on the membrane batch[27]. The excellent performance of the new electrode probably resulted from a synergistic interplay of factors that coupled the redox features of **1** with the MWCNT-enabled nanoscale structure and electrical wiring of the hybrid material. The Tafel-like behaviour (Fig. 3f), with no deviation from linearity up to $\eta = 0.6$ V, is a consequence of the exponential dependence of the quasi-stationary currents on the overpotential, shown in Fig. 3e (inset), and again confirmed the attainment of a well-behaved ohmic contact to the ITO.

Conclusions

Although homogeneous studies of water splitting demonstrated the advantage of storing multiple redox equivalents in a single catalyst[28], our results address the importance of hybrid interfaces and/or contacts to control and promote electron-transfer events at heterogeneous surfaces. In conclusion, the use of tailored and functionalized MWCNTs enables the design of water-splitting electrodes with remarkably improved efficiency, operative voltage, current density and operational stability. These results open new avenues for innovative materials design to address the dimensionality, properties and morphology of the nanoscaffold as powerful parameters in terms of efficiency and cost optimization for a viable hydrogen economy.

Methods

The MWCNTs used in this study are commercially available and were purchased from Nanostructured & Amorphous Materials (1240XH, 95%, outer diameter 20–30 nm). The metal content of pristine MWCNT was determined by atomic absorption spectrometry to give a composition of 7.95% Fe and 2.20% Ni (ref. 29). AC was purchased from Sigma-Aldrich (carbon nanopowder ≥99%). **1** was prepared according to the literature procedure[11]. **MWCNT-dend** was prepared as described previously[20]. All the solvents and the reagents for **1**, **MWCNT-dend** and **AC-dend** syntheses were purchased from Sigma Aldrich. ITO electrodes were purchased from Zaot Italy. PBS solution (pH 7.0) was prepared using MilliQ water and PBS tablets purchased from Sigma Aldrich (Biochemika).

TGAs were performed on a TGA Q500 (TA Instruments) and recorded under nitrogen or under air, on equilibration at 100 °C, followed by a ramp of 10 °C min^{-1} up to 1,000 °C. Micro-Raman spectra were recorded with an inVia Renishaw spectrometer equipped with helium–neon (632.8 nm) and argon (488 nm) lasers. The laser beam was focused on an area of about 2 × 2 μm with power lower than 1 mW. HRTEM and STEM images were obtained with a JEOL JEM2010F transmission electron microscope operated at 200 kV. STEM images were obtained using the high-angle annular dark-field detector, so the images show a mass–thickness contrast or *Z*-contrast. To obtain the elemental distribution maps (STEM–XEDS maps), the XEDS detector was coupled to the STEM detector. SAXS measurements were conducted at the Austrian SAXS beamline of the electron-storage ring ELETTRA using 8 keV photon energy (see Supplementary Information). For the measurements, the various sample solutions were placed in 1.5 mm diameter glass capillaries (Hilgenberg, Germany) held in a cell to maintain a temperature of 25 °C. XPS spectra were recorded at the beamline for advanced dichroism (BACH) at ELETTRA using 461 eV photon energy, with an energy resolution of 0.1 eV. The material was supported on ITO substrates by drop casting 500 μl of 1 mg ml^{-1} aqueous solutions. SEM micrographs were collected by a Zeiss SUPRA 40VP instrument, with an accelerating voltage of 10 kV, using electrodes prepared in the same way as those for electrochemical measurements. AFM images were obtained using a NT–MDT SPM Solver P47H–PRO instrument operated in tapping mode and in air. Micrographs were recorded on different sample areas to check the surface homogeneity.

Synthesis of 1@MWCNT. Straightforward metathesis techniques were adopted in water solution to anchor **1** to the positively charged **MWCNT-dend**. In all experiments 5 mg of **MWCNT-dend** were mixed with a different amount of **1** in aqueous solution at pH 5 (see Supplementary Information). The mixture was stirred overnight and the material recovered by filtration on a Millipore system (filter JHWP 0.45 μm).

Synthesis of 1@AC. Positively charged PAMAM-modified amorphous carbon (**AC-dend**) was obtained by covalent functionalization of amorphous carbon, using the conditions reported for MWCNT[20]. **1** was supported on the material by metathesis techniques, using 5 mg of **AC-dend** in the presence of $\mathbf{Li_{10}1}$ in aqueous solution at pH 5 (Supplementary Scheme S2 and Table S3). The solution was stirred overnight and the material recovered by filtration on a Millipore system (filter JHWP 0.45 μm). As a blank experiment, pristine amorphous carbon (**AC-pristine** (5 mg)) was mixed with $\mathbf{Li_{10}1}$ in aqueous solution at pH 5 (Supplementary Table S3). As described above, the solution was stirred overnight and then the material recovered by filtration on a Millipore system (filter JHWP 0.45 μm).

Electrochemistry. ITO electrodes doped with **1@MWCNT**, **1**, **MWCNT-dend** and **1@AC** were prepared by casting 100 μl of an aqueous mixture (1 mg ml^{-1}) of each sample on a 1 cm^2 ITO surface.

Voltammograms and chronoamperometries of the substrate were recorded with an AMEL Model 552 potentiostat or a custom-made fast potentiostat controlled by an AMEL Model 568 function generator. Data acquisition was carried out with a Nicolet Model 3091 digital oscilloscope interfaced with a personal computer. All the experiments were carried out in a polytetrafluoroethylene cell with a 6 mm diameter aperture with an O-ring placed on top of the substrates and tightened using two connecting screws. The cell was also equipped with a platinum wire as the counter electrode and an Ag/AgCl (3 M KCl) reference electrode.

The oxygen-evolving activity of the **1@MWCNT** film was measured by SECM using a 910B scanning electrochemical microscope (CHI Instruments, Austin). The cell was mounted on the SECM stage. The experimental set-up used an ultramicroelectrode tip as the basis for a Clark membrane electrode to effect the real-time sensing oxygen concentration in solution using the oxygen-reduction signal. The SECM tip was a home-made μ-Clark electrode[30] (see 'Fabrication of μ-Clark electrode' in the Supporting Information). All the potentials were referred to the Ag/AgCl electrode, the stability of which was checked periodically during the experiment.

Received 15 March 2010; accepted 15 June 2010; published online 8 August 2010

References

1. Balzani, V., Credi, A. & Venturi, M. Photochemical conversion of solar energy. *ChemSusChem* **1,** 26–58 (2008).
2. Gray, H. B. Powering the planet with solar fuel. *Nature Chem.* **1,** 7 (2009).
3. Lewis, N. S. & Nocera, D. G. Powering the planet: chemical challenges in solar energy utilization. *Proc. Natl Acad. Sci. USA* **103,** 15729–15735 (2006).
4. Meyer, T. J. Catalysis: the art of splitting water. *Nature* **451,** 778–779 (2008).
5. Loll, B., Kern, J., Saenger, W., Zouni, A. & Biesiadka, J. Towards complete cofactor arrangement in the 3.0 Å resolution structure of photosystem II. *Nature* **438,** 1040–1044 (2005).

6. Ferreira, K. N., Iverson, T. M., Maghlaoui, K., Barber, J. & Iwata, S. Architecture of the photosynthetic oxygen-evolving center. *Science* **303,** 1831–1838 (2004).
7. Yano, J. *et al.* Where water is oxidized to dioxygen: structure of the photosynthetic Mn_4Ca cluster. *Science* **314,** 821–825 (2006).
8. Que, L. Jr & Tolman, W. B. Biologically inspired oxidation catalysis. *Nature* **455,** 333–340 (2008).
9. Rappaport, F., Guergova-Kuras, M., Nixon, P. J., Diner, B. A. & Lavergne, J. Kinetics and pathways of charge recombination in photosystem II. *Biochemistry* **41,** 8518–8527 (2002).
10. Ananyev, G. & Dismukes, G. C. How fast can photosystem II split water? Kinetic performance at high and low frequencies. *Photosynth. Res.* **84,** 355–365 (2005).
11. Sartorel, A. *et al.* Polyoxometalate embedding of a catalytically active tetraruthenium(IV)-oxo-core by template-directed metalation of $[\gamma\text{-}SiW_{10}O_{36}]^{8-}$. *J. Am. Chem. Soc.* **130,** 5006–5007 (2008).
12. Geletii, Y. V. *et al.* An all-inorganic, stable, and highly active tetraruthenium homogeneous catalyst for water oxidation. *Angew. Chem. Int. Ed.* **47,** 3896–3899 (2008).
13. Sartorel, A. *et al.* Water oxidation at a tetraruthenate core stabilized by polyoxometalate ligands: experimental and computational evidence to trace the competent intermediates. *J. Am. Chem. Soc.* **131,** 16051–16053 (2009).
14. Liu, F. *et al.* Mechanisms of water oxidation from the blue dimer to photosystem II. *Inorg. Chem.* **47,** 1727–1752 (2008).
15. Kanan, M. K. & Nocera, D. G. *In situ* formation of an oxygen-evolving catalyst in neutral water containing phosphate and Co^{2+}. *Science* **321,** 1072–1075 (2008).
16. Mola, J. *et al.* Ru-Hbpp-based water-oxidation catalysts anchored on conducting solid supports. *Angew. Chem. Int. Ed.* **47,** 5830–5832 (2008).
17. Brimblecombe, R., Swiegers, G. F., Dismukes, G. C. & Spiccia, L. Sustained water oxidation photocatalysis by a bioinspired manganese cluster. *Angew. Chem. Int. Ed.* **47,** 7335–7338 (2008).
18. Cracknell, J. A., Vincent, K. A. & Armstrong, F. A. Enzymes as working or inspirational electrocatalysts for fuel cells and electrolysis. *Chem. Rev.* **108,** 2439–2461 (2008).
19. Gong, K., Du, F., Xia, Z., Durstock, M. & Dai, L. Nitrogen-doped carbon nanotube arrays with high electrocatalytic activity for oxygen reduction. *Science* **323,** 760–764 (2009).
20. Herrero, M. A. *et al.* Synthesis and characterization of a carbon nanotube–dendron series for efficient siRNA delivery *J. Am. Chem. Soc.* **131,** 9843–9848 (2009).
21. Mašek, K. *et al.* SRPES investigation of tungsten oxide in different oxidation states. *Surf. Sci.* **600,** 1624–1627 (2006).
22. Moulder, J. F., Stickle, W. F., Sobol, P. E. & Bomben, K. D. *Handbook of X-Ray Photoelectron Spectroscopy* (Perkin-Elmer, 1992).
23. Mackiewicz, N. *et al.* Supramolecular self-assembly of amphiphiles on carbon nanotubes: a versatile strategy for the construction of CNT/metal nanohybrids, application to electrocatalysis. *J. Am. Chem. Soc.* **130,** 8110–8111 (2008).
24. Bi, L.-H. *et al.* Organo-ruthenium supported heteropolytungstates: synthesis, structure, electrochemistry, and oxidation catalysis. *Inorg. Chem.* **48,** 10068–10077 (2009).
25. Wightman, R. M. Probing cellular chemistry in biological systems with microelectrodes. *Science* **311,** 1570–1574 (2006).
26. Lutterman, D. A., Surendranath, Y. & Nocera, D. G. A self-healing oxygen-evolving catalyst. *J. Am. Chem. Soc.* **131,** 3838–3839 (2009).
27. Brimblecombe, R. *et al.* Sustained water oxidation by $[Mn_4O_4]^{7+}$ core complexes inspired by oxygenic photosynthesis. *Inorg. Chem.* **48,** 7269–7279 (2009).
28. Tinker, L. L., McDaniel, N. D. & Bernhard, S. Progress towards solar-powered homogeneous water photolysis. *J. Mater. Chem.* **19,** 3328–3337 (2009).
29. Lacerda, L. *et al.* Dynamic imaging of functionalized multi-walled carbon nanotube systemic circulation and urinary excretion. *Adv. Mat.* **20,** 225–230 (2008).
30. Carano, M., Holt, K. B. & Bard, A. J. Scanning electrochemical microscopy 49. Gas-phase scanning electrochemical microscopy measurements with a Clark oxygen ultramicroelectrode. *Anal. Chem.* **75,** 5071–5079 (2003).

Acknowledgements

We thank M. Meneghetti for assistance with the RAMAN spectroscopy and discussion of the data. Financial support from Consiglio Nazionale delle Ricerche (CNR), Consorzio Interuniversitario Nazionale per la Scienza e Tecnologia dei Materiali (INSTM), Ministero dell'Istruzione, dell'Università e della Ricerca (MIUR, PRIN Contract No. 20085M27SS), University of Padova (Progetto Strategico 2008, HELIOS, prot. STPD08RCX) the European Science Foundation's Cooperation in Science and Technology D40 action, Fondazione Cassa di Risparmio in Bologna and the University of Bologna is acknowledged.

Author contributions

F.M.T. performed the synthetic tasks, optimized the deposition protocol and coordinated the characterization and electrocatalytic experiments; A.S. and M.C. contributed to the design, synthesis and characterization of the POM interface; C.M. carried out the SEM and AFM, and analysed the data; B.R.G. performed the HRTEM and STEM analyses; H.A. carried out the SAXS and analysed the data; L.C., A.G. and P.P. performed the XPS and analysed the data; F.P., M.M., S.R. and M.I. performed and analysed the electrochemistry experiments; T.D.R. discussed and supervised the functionalization of carbon nanostructure; G. Scorrano helped with the design and discussion of the experiments; G. Scoles helped with the design and discussion of the experiments, and contributed to writing the manuscript; M.P. and M.B. planned and supervised the research, analysed the data and co-wrote the manuscript.

Additional information

The authors declare no competing financial interests. Supplementary information accompanies this paper at www.nature.com/naturechemistry. Reprints and permission information is available online at http://npg.nature.com/reprintsandpermissions/. Correspondence and requests for materials should be addressed to M.P. and M.B.